Phase profiles of microwave magnetic envelope solitons

J. M. Nash,[a] P. Kabos,[b] R. Staudinger, and C. E. Patton
Colorado State University, Fort Collins, Colorado 80523

(Received 2 September 1997; accepted for publication 18 November 1997)

A new method for the analysis of microwave magnetic envelope (MME) solitons has been developed. This method is based on the determination and analysis of output microwave pulse phase profiles. Simple analytical results based on the nonlinear Schrödinger equation show that MME soliton phase profiles contain the necessary and sufficient information needed to define a particular pulse as a linear dispersive pulse or a fully formed soliton. The effects are demonstrated both theoretically and experimentally for magnetostatic backward volume wave and magnetostatic surface wave pulse signals. Theoretical phase profiles are considered for Gaussian, hyperbolic secant, and rectangular pulse shapes. Experimental profiles are obtained for rectangular input pulses. The measured phase profiles compare favorably with the numerical results. Both the data and the theory show that a constant phase profile across the pulse provides a consistent and quantitative criterion for an MME soliton. © *1998 American Institute of Physics.* [S0021-8979(98)03305-2]

I. INTRODUCTION

Microwave magnetic envelope (MME) solitons were first predicted by Zvezdin and Popkov,[1] based on an analysis of the nonlinear Schrödinger equation. The first observation of MME solitons formed from magnetostatic wave (MSW) pulses was later reported by Kalinikos, Kovshikov, and Slavin.[2] Since then, strong experimental and theoretical evidence has been presented which indicates that, under the right conditions, MME solitons can form and propagate in magnetic thin films.[3–15] Solitons in magnetic films hold promise for radar signal processing applications. Reference 15, for example, describes a generator which can produce a train of soliton pulses which is maintained without a change in pulse shape of decay in amplitude for tens of microseconds.

Although the above works were for different magnetic thin films parameters and external magnetic field orientations, they all depended on some determination of whether or not a given output pulse was a soliton. Five basic techniques were used in Refs. 2–15 to make this identification, each based on measurements of different output pulse characteristics. These techniques involved (i) the evolution in the shape of the pulse envelope,[2,7] (ii) the output peak power versus the input peak power response,[3,7,8] (iii) the effect of collision between two pulses,[8,12] (iv) decay properties,[12,14] and (v) phase profiles.[6,11,13,15]

This article presents a discussion of the phase profile approach to soliton identification. Some preliminary theoretical and experimental results were presented in Refs. 11 and 13. The basic idea is based on the result that MME pulses subject to dispersion or the effects of the nonlinear response alone will exhibit characteristic phase profiles as well as the usual amplitude profiles. These phase profiles will have characteristic dependences which depend on the signs of the dispersion and nonlinear response coefficients. When the dispersion and the nonlinear response are such that an MME soliton is formed, the phase profile across the pulse will be constant. That is, the cw signal inside the MME wave packet will be purely harmonic and not subject to additional phase shifts.

II. MME SOLITON IDENTIFICATION

The MME soliton experiments of interest here are described in detail by Chen *et al.*[7] In short, a square microwave pulse is applied to the input port of a microstrip transducer structure, such as the one shown in Fig. 1. A long and narrow strip from a single crystal low loss yttrium iron garnet (YIG) film is placed YIG-side down across the two narrow sections of the striplines. These narrow sections act as input and output transducers for the generation and detection of MME pulses. The entire structure is placed between the poles of an electromagnet so that the magnetic film is subject to a static applied field.

For the field parallel to the propagation direction, as in Fig. 1, one has the magnetostatic backward volume wave (MSBVW) configuration discovered by Damon and Eshbach.[16] The propagation of MME solitons for this case has been studied in detail by Chen *et al.*,[7] Kalinikos *et al.*,[12] and Xia *et al.*[14] If the static field is applied perpendicular to the plane of the YIG film, one has the forward volume wave configuration first analyzed by Damon and Van der Vaart.[17] This configuration was used for the first magnetic film soliton experiments by Kalinikos and co-workers, as described in Ref. 2. For these two configurations, the so-called Lighthill criterion[18] is satisfied and the relationship between the dispersion and the nonlinear response is such that MME solitons can be formed and propagated in low loss YIG films. References 2–5 and 7–15 describe a wide variety of experimental results for these cases. For a third configuration, in which the external field is applied in the plane of the YIG film but the propagation direction is perpendicular to the

[a]Present address: Department of Information Systems, Montemorelos University, Montemorelos, Nuevo Leon, Mexico.
[b]Electronic mail: kabos@lamar.colostate.edu

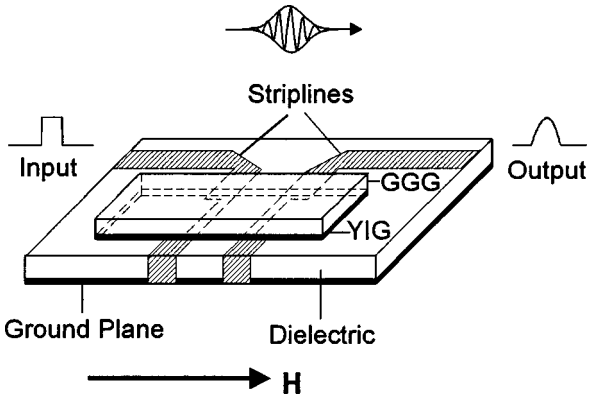

FIG. 1. Diagram of the yttrium iron garnet (YIG) film magnetostatic wave (MSW) propagation structure. The long and narrow YIG film on the gadolinium gallium garnet (GGG) substrate supports the propagating MSW pulse signal from left to right as indicated. The film is positioned YIG side down over the two strip line transducers as shown. The strip line circuits are on the bottom single ground plane microwave dielectric support structure and provide the input pulse excitation and output pulse detection. The figure shows a static magnetic field H applied parallel to the propagation direction.

field, the Lighthill criterion is not satisfied.[7] The fundamental modes of propagation which are supported now consists of magnetostatic surface wave or MSSW excitations.[16] In this case, MME solitons cannot be formed. The focus in this article will be on MSBVW and MSSW wave packets and the phase features for soliton and nonsoliton pulses. The differences between these configurations will be discussed shortly.

Figure 2 is reproduced from Fig. 7 of Ref. 7. This figure shows the results of a typical magnetostatic backward volume wave MME soliton experiment. Graphs (a)–(d) show input and output profiles of detected power versus time for

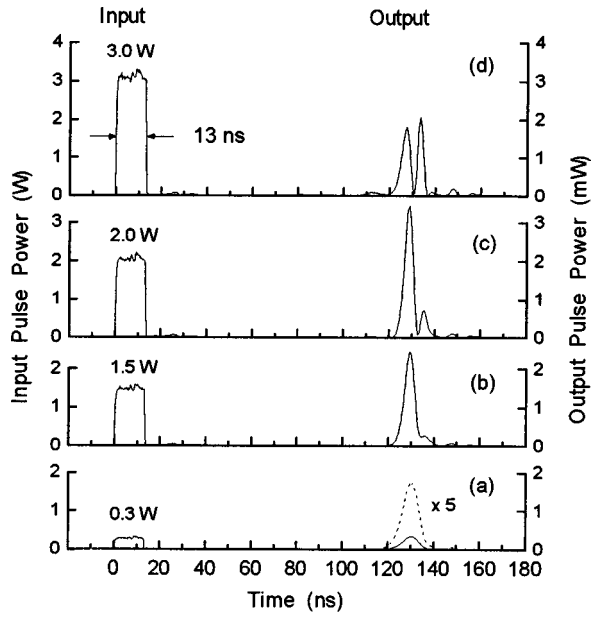

FIG. 2. Input and output profiles of detected power vs time for the YIG film and transducer structure of Fig. 1 and four different input power levels as indicated. The film thickness was 7.2 μm and the external applied field was 1343 Oe. The carrier frequency was 5.8 GHz and the input pulse width was held constant at 13 ns. The dashed curve for output profile (a) shows the pulse with the vertical response expanded by a factor of 5. This figure is the same as Fig. 7 in Ref. 7.

the YIG film transducer structure of Fig. 1 in the MSBVW configuration for different input power levels as indicated. The film thickness was 7.2 μm and the external applied field was 1343 Oe. The carrier frequency was 5.8 GHz and the input pulse width was held constant at 13 ns. The dashed curve for output profile (a) shows the pulse with the vertical response expanded by a factor of 5. The steepening and narrowing of the output pulse profile seen in traces (b), (c), and (d) were used to demonstrate MME soliton formation.

The steepening and narrowing of the pulses shown in Fig. 2 provide one qualitative indication of soliton formation. There are further characteristics which can be exploited to support the formation of solitons in these experiments. One such characteristic is obtained from measurements of the variation in the peak output power P_{out} as a function of the peak input power P_{in}. A typical P_{out} vs P_{in} measurement gives a response curve with three characteristic regions.[7,8,14] The first region corresponds to low input power levels and consists of the expected linear response. At some relatively low power level, however, this linear response changes to a nonlinear response in which the output peak power increases more rapidly than before. The response in this second region is still monotonic and more-or-less linear. At even higher power levels, one has a P_{out} vs P_{in} response in which P_{out} goes through a maximum and then decreases. The onset of the nonlinear response in the second region corresponds to the formation of order one solitons and the steepening and narrowing shown in Fig. 2. The peak effect in the third region is connected with the formation of higher order solitons, the evolution of additional peaks in the pulse profiles, and the kind of response shown in traces (c) and (d) of Fig. 2. The power at the boundary between the first to the second region may be taken to represent the threshold input power for soliton formation. Such threshold powers have been found to be in reasonable agreement with predictions based on the nonlinear Schrödinger (NLS) equation and predictions from inverse scattering theory.[10] Discussions of threshold powers and connections with soliton theory are given in Refs. 7, 8, 10, and 14.

The third technique for soliton identification is based on the property that solitons which undergo collisions will remain unchanged, except for an overall shift in phase. Measurements of soliton pulse profiles before and after collision have been reported in Refs. 8 and 12. The profiles of the two pulses were found to be unaffected by the collision.

The fourth technique concerns decay. As discussed in Refs. 10 and 12, soliton pulses are expected to decay more rapidly than linear pulses. Reference 14 provides the most recent quantitative measurements and theoretical analyses of decay effects. Decay measurements require data for many pulses as a function of propagation time and power level. It is possible to follow the formation of a MME soliton on the basis of detailed decay data for both the pulse amplitude and the integrated pulse energy. The results are based on many different measurements and not on a single pulse signal.

In contrast with the above approaches, phase profiles provide a direct indication of the soliton or nonsoliton nature of a single pulse. Recall that the wave packet which is applied to the input transducer in Fig. 1 consists of a carrier

signal at a specified microwave frequency and an envelope defined by the input pulse shape. As this microwave pulse energy is coupled into the film, an MSW pulse is formed and propagated. The shape of the pulse will evolve in some form as indicated by the data in Fig. 2. At the same time, there will be some evolution in the relative phase of the carrier signal inside the pulse envelope. One may define the deviation in phase at a particular point on the pulse signal, relative to the phase for an undisturbed carrier for a perfectly linear and dispersion free medium, as the phase profile for the pulse. Hence, there are two profiles for the pulse signal, the one for amplitude or power as shown in Fig. 2 and one for phase. The objective of this report is to describe the physical effects which determine the various phase profiles which can be obtained from MSW pulses and to examine such phase profiles both theoretically and experimentally.

Why consider phase? The other approaches given above for soliton identification present various problems. The ''steepening and narrowing'' characteristic is purely qualitative. There are more serious problems as well. Pulse distortions can occur, for example, for input pulses which contain Fourier components which extend outside the MSW band.

The threshold approach is subject to the problem of poorly defined thresholds because the change from the linear to the nonlinear regime can be rather gradual.[10] The problem here is that, even though the threshold for soliton formation may be well defined, the time required for the soliton to actually form may be rather long on the time scale of practical microwave pulse experiments with YIG films. This means that the onset point may be difficult to measure with high accuracy.

There are also problems with the collision criterion. To date, only the output pulse profiles have been compared before and after collision. Such results are unable to distinguish uniquely between collisions of pulses which are in the low power linear regime and pulses which are solitons. Both linear pulses and soliton pulses are expected to maintain their shapes upon collision.

Decay measurements provide perhaps the best method to date to clearly and quantitatively define an MME soliton. In order to do so, however, it is necessary to perform detailed measurements of both the amplitude decay and the decay in the total energy of the pulse as a function of propagation distance.[14] Such experiments are tedious and time consuming.

A quantitative criteria for soliton pulses based on phase profiles would provide a clear and relatively simple way to identify solitons. This approach was applied to a limited extent to the MSSW dark soliton observed in Ref. 6 and to MSBVW soliton trains in Ref. 15. For the dark solitons, measurements of the phase across the central part of the output pulse profile showed that there was a phase shift of π across the middle of the pulse when a dark soliton was fully formed. For the soliton train measurements, each soliton in the pulse train was found to have a constant phase profile. The phase approach to soliton identification does not suffer from the problems noted above for amplitude or power profiles. Only one output pulse needs to be measured, and the phase profile of the output pulse is a direct consequence of soliton formation.

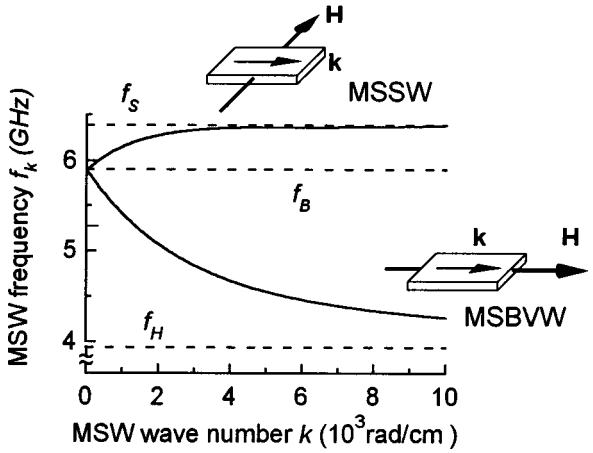

FIG. 3. Dispersion diagrams of magnetostatic wave (MSW) frequency f_k vs wave number k for the two basic MSW configurations for in-plane magnetized films, the magnetostatic surface wave (MSSW) configuration, and the magnetostatic backward volume wave (MSBVW) configuration. The relative orientations of the net static magnetic field **H** and the wave vector **k** are shown by the inset diagrams for the two dispersion curves. The curves shown are actual calculated curves for a 7.2-μm-thick yttrium iron garnet film with a field H of 1407 Oe. The horizontal dashed lines indicate the three characteristic MSW limit frequencies f_S, f_B, and f_H.

The results below are divided into four sections. Section III presents basic considerations for linear and nonlinear magnetostatic wave pulse propagation, dispersion effects, and nonlinear effects. Section IV and V present theoretical results on phase profiles and Sec. VI presents experimental results. The presentation here is for bright pulses only. Dark pulses are not considered.

III. LINEAR AND NONLINEAR MSW EXCITATIONS

The starting point for the discussion of MME wave packets is the frequency ω_k vs wave number k response for the lowest order dispersion branch of the fundamental magnetostatic wave excitation for the thin film geometry of interest. Figure 3 shows representative MSSW and MSBVW small signal dispersion curves for an in-plane magnetized 7.2-μm-thick YIG film with an in-plane static magnetic field H of 1407 Oe. The top curve is for the MSSW case and propagation perpendicular to the in-plane static magnetic field and static magnetization direction. The bottom curve is for the MSBVW case and propagation parallel to the static field. The inset diagrams show these configurations. The above curves may be obtained directly from the theory of magnetostatic waves developed by Damon and Eshbach.[16] The Damon–Eshbach theory has been revisited in a recent article by Hurben and Patton.[19] The horizontal dashed lines indicate the three characteristic MSW limit frequencies f_S, f_B, and f_H.

For the present purposes, two properties of the dispersion curves in Fig. 3 are important: (1) the common limit frequency f_B for zero wave number and (2) the different shapes and curvatures of the dispersion relations. First consider the common f_B frequency point. This frequency corre-

sponds to the uniform mode ferromagnetic resonance frequency for an in-plane magnetized film. From the original Kittel analysis,[20] this ferromagnetic resonance (FMR) frequency is given by

$$f_B = \omega_B/2\pi = (|\gamma|/2\pi)\sqrt{H(H+4\pi M_s)}. \tag{1}$$

Equation (1), γ denotes the electron gyromagnetic ratio and $4\pi M_s$ denotes the saturation induction of the material. For YIG materials, γ is close to the free electron value of -1.76×10^6 rad/Oe and one has $4\pi M_s \approx 1750$ G. In practical units, one also has $|\gamma|/2\pi = 2.8$ GHz/kOe. Equation (1) and the analysis to follow is based on cgs or Gaussian units. Frequencies specified in terms of f symbols are in Hz or GHz and frequencies specified in terms of ω are taken to be in rad/s.

The FMR frequency in Eq. (1) is important to the nonlinear frequency response for MSW excitations. Typically, MSW excitations are utilized at relatively small values of the wave number k on the order of 100 rad/cm or so. On the scale of the dispersion curves in Fig. 3, this range of wave numbers is very close to $k=0$. This means that one may estimate the frequency shift for MSW excitations of large amplitude from the M_s dependence of the FMR frequency in Eq. (1). This procedure will be described shortly. The point to be noted here is that this shift will be negative for both MSSW and MSBVW excitations. The direction of this shift is clear from the M_s dependence in Eq. (1). The effective static magnetization will decrease as the FMR precession angle increases. This decrease translates into a decrease in the FMR frequency and a corresponding downshift in the dispersion curves of Fig. 3.

Turn now to the dispersion curves in Fig. 3. It will be useful to introduce a dispersion coefficient D, defined as

$$D = \partial^2\omega_k/\partial k^2. \tag{2}$$

For the MSSW case in Fig. 3(a), f_k initially increases from the f_B point as k increases, the dispersion curve has negative curvature, and D is negative. For the MSBVW case in Fig. 3(b), f_k initially decreases from the f_B point as k increases, the dispersion curve has positive curvature, and D is positive. These opposite signs for D for MSSW and MSBVW excitations play a critical role in the nonlinear pulse response characteristics. Recall from the brief discussion above that the nonlinear frequency response, that is, the change in the MSW frequency with signal amplitude, for the two cases is about the same.

In addition to the dispersion parameter D, a second important MSW property derives from the dispersion curve. This is the group velocity v_g, which is the speed of propagation for a linear MSW wave which is reasonably wide spatially or temporally, and reasonably narrow in frequency content. This group velocity is determined by the slope of the ω_k vs k dispersion relation at a given operating point according to $\nu_g = \partial\omega_k/\partial k$. A typical low amplitude or linear wave packet will travel at the group velocity ν_g and spread as it propagates. The spreading is due to the nonzero dispersion coefficient D.

Now consider the nonlinear response. The dispersion curves of Fig. 3 are strictly valid only in the limit of a vanishingly small dynamic magnetization response. As the amplitude of the dynamic magnetization components increase, there is a corresponding change in the MSW frequency. These nonlinear shifts in the MSW frequency have been theoretically investigated by a number of authors. The simplest approach, first used by Zvezdin and Popkov,[1] is to approximate the nonlinear frequency shift for a MSW signal at a relatively low wave number by the corresponding shift in the FMR frequency with the amplitude of the uniform mode or $k=0$ response. Operational equations for this shift are summarized in Ref. 7.

The remainder of this section will establish basic equations for the dynamic magnetization **m** associated with an MME wave packet, define a complex dimension less scalar wave packet amplitude function u, and introduce the operational nonlinear differential equation, the nonlinear Schrödinger (NLS) equation, which will be used to evaluate the amplitude and phase properties of these linear wave packets and soliton pulses of interest here.

One begins with the dynamic magnetization response for a general MSW one dimensional wave packet. The vector dynamic magnetization is written in the form

$$\mathbf{m} = \mathbf{m}_0(z,t)e^{-i(kz-\omega_k t)}. \tag{3}$$

The z direction is taken as the direction of propagation. For MSBVW signals, the dynamic magnetization **m** is superimposed on a z-directed static magnetization vector $\mathbf{M}_z = M_z\hat{\mathbf{z}}$. For MSSW signals, the dynamic magnetization **m** is superimposed on static magnetization vector which is still in the plane of the YIG film but transverse to the propagation direction. If this transverse direction is taken as the x direction, the static magnetization vector for the MSSW configuration is given as $\mathbf{M}_x = M_x\hat{\mathbf{x}}$. In general, it is assumed that the total magnetization vector **M** is conserved such that $|M| = M_s$ is true, where M_s represents the saturation magnetization of the material.

The transverse dynamic magnetization response may be further broken down according to $\mathbf{m}_0 = m_{\text{in}}\hat{\mathbf{x}} + m_{\text{out}}\hat{\mathbf{y}}$ for the backward volume wave case and as $\mathbf{m}_0 = m_{\text{in}}\hat{\mathbf{z}} + m_{\text{out}}\hat{\mathbf{y}}$ for the magnetostatic surface wave configuration. The m_{in} and m_{out} represent complex scalar dynamic magnetization response functions for the in-plane and out-of-plane components of $\mathbf{m}_0(z,t)$.

If the wave number k is small, such that $k/L \ll 1$ is satisfied, where L represents the film thickness, the ratio of the out-of-plane component of the dynamic magnetization $\mathbf{m}_0(z,t), m_{\text{out}}$, to the transverse in plane component m_{in} is approximately the same as obtained for free precession ferromagnetic resonance (FMR) for an in-plane magnetized thin film. This ratio is given by

$$\frac{m_{\text{out}}}{m_{\text{in}}} = \mp i\,\frac{H}{H+4\pi M_s}. \tag{4}$$

The upper and lower signs on the right hand side apply to the MSBVW and MSSW cases, respectively, and are chosen such that the sense of precession of the dynamic magnetization is in the Larmor sense. Note that $m_{\text{in}}(z,t)$ and $m_{\text{out}}(z,t)$ represent wave packet functions in their own right. These functions are scalar and complex.

Return now to the nonlinear response. This response may be characterized in terms of the shift in the MSW frequency with the amplitude of the MSW signal. The nonlinear coefficient, N, is a measure of the shift in the actual spin wave or MSW frequency with the amplitude of the dynamic magnetization response. The standard approach is to assume that this shift is approximately the same as the shift in the FMR frequency. One introduces a reduced, dimension less, complex scalar function parameter $u(z,t)$ which is related to the dynamic magnetization response. For the present purposes, this connection will be taken as

$$m_{\text{in}}(z,t)=u(z,t)M_s. \tag{5}$$

With m_{out} defined through Eq. (4), the complex dynamic response $\mathbf{m}_0(z,t)$ is now defined in terms of a scalar complex wave packet envelope function $u(z,t)$. This connection between $\mathbf{m}_0(z,t)$ and $u(z,t)$ is the same as defined in Ref. 7. Note that because of the M_s factor in Eq. (5), the numerical values for $u(z,t)$ will correspond roughly to the ratio $|\mathbf{m}_0(z,t)|/M_s$.

With $u(z,t)$ now given in terms of $\mathbf{m}_0(z,t)$, one may now establish a nonlinear response coefficient N according to

$$N=\partial\omega_k/\partial|u|^2|_{u=0}. \tag{6}$$

A useful analytical expression for N for the MSBVW and MSSW cases may be obtained in a simple way. One first replaces ω_k in Eq. (6) with ω_B. One then replaces M_s in Eq. (1) with an effective z-component static magnetization M_s given by

$$M_z=\sqrt{M_s^2-|m_{\text{in}}^2|-|m_{\text{out}}^2|}\approx M_s-\frac{|m_{\text{in}}^2|+|m_{\text{out}}^2|}{2M_s}. \tag{7}$$

Finally, one uses the connection between u and m_{in} and m_{out} given above, and evaluates N according to

$$N=\partial\omega_B/\partial|u|^2|_{u=0}. \tag{8}$$

The result of these operations is a closed form expression for N given by

$$N=-\frac{|\gamma|4\pi M_sH}{4(H+4\pi M_s)}\left[1+\left(\frac{H}{H+4\pi M_s}\right)^2\right]. \tag{9}$$

This is the same result as stated by Zvezdin and Popkov in Ref. 1.

The operational parameters for linear and nonlinear MSW wave packet propagation have now been established. Actual solutions for wave packet are generally obtained from some variation of the nonlinear Schrödinger equation. One useful form of this equation, based on the harmonic convention of Eq. (3), may be written as

$$i\left(\frac{\partial u}{\partial t}+\nu_g\frac{\partial u}{\partial z}+\eta u\right)-\frac{1}{2}D\frac{\partial^2u}{\partial z^2}+N|u|^2u=0. \tag{10}$$

The only parameter in Eq. (10) has not yet been established is the relaxation rate η. This relaxation rate parameter describes the losses or damping of the microwave magnetic response. This relaxation rate is related to the usual half-power ferromagnetic resonance line width ΔH according to $\Delta H=2\eta/|\gamma|$.

The general approach is to prescribe some real input envelope function $u(z,t=0)$ and obtain analytic or numerical solutions for $u(z,t)$. These complex $u(z,t)$ functions may be expressed in the form

$$u(z,t)=\mu(z,t)e^{i\theta(z,t)}, \tag{11}$$

where both $\mu(z,t)$ and $\theta(z,t)$ are taken as real functions. The $\mu(z,t)$ function represents the amplitude of the MSW wave packet and $\theta(z,t)$ represents the phase of the local carrier signal inside the wave packet relative to the original carrier specified through Eq. (3). For a purely linear and nondispersive wave packet, the phase function $\theta(z,t)$ will be identically zero. As will be demonstrated below, dispersion and nonlinear frequency shifts with local amplitude introduce characteristic phase profiles which can be related to soliton formation in a simple and intuitive, yet quantitative way.

For the theoretical results to be presented in the next two sections, numerical values of the D and N parameters established above have been used which represent typical values for MSW wave packets. The physical basis for these values is discussed in Refs. 6–8 and 12, among others. Profiles have been computed for $D=\pm3\times10^3$ cm^2/rad s and $N=\pm7.4\times10^9$ rad/s. The computations were done for zero damping and zero group velocity. Real MSW wave packets will, of course, be moving and be subject to decay because of damping. The objective of the next two sections, however, is to demonstrate the effects of D and N on phase profiles. In order to do this in the simplest way, propagation and decay have been set to zero. Wave packet amplitudes and widths have also been adjusted to optimally demonstrate the effects on phase profiles. These numerics will be considered shortly.

IV. DISPERSIVE AND NONLINEAR GAUSSIAN WAVE PACKETS

The purpose of this section is to use a particularly simple and analytically solvable input envelope $u(z,t=0)$ function, and obtain analytical $u(z,t)$ solutions to the NLS equation for the two cases: (a) dispersion only, with $N=0$, and both signs for the D parameter, (b) nonlinear response only, with $D=0$, and both signs for the N parameter. These computations will utilize a Gaussian input pulse.

Consider a real $u(z,t=0)$ input pulse of the form

$$u(z,t=0)=u_0e^{-z^2/4z_0^2}, \tag{12}$$

where u_0 is the amplitude of the pulse and z_0 is a width parameter for the pulse. With the group velocity ν_g, the damping η, and the nonlinear response coefficient N set to zero, Eq. (10) reduces to

$$i\frac{\partial u}{\partial t}-\frac{1}{2}D\frac{\partial^2u}{\partial z^2}=0. \tag{13}$$

Subject to the initial condition of Eq. (12), Eq. (13) has a complex $u(z,t)$ dispersion only solution with the separate amplitude and phase functions $\mu(z,t)$ and $\theta(z,t)$ given by

$$\mu_D(z,t)=\frac{2u_0z_0}{(D^2t^2+4z_0^4)^{1/4}}e^{-z_0^2z^2/(D^2t^2+4z_0^4)} \tag{14}$$

and

$$\theta_D(z,t)=\frac{1}{2}\tan^{-1}\left(\frac{Dt}{2z_0^2}\right)-\frac{Dtz^2}{2(D^2t^2+4z_0^4)}. \tag{15}$$

Notice that both the amplitude and the phase functions depend on D. It is clear from the form of Eq. (14) that the $\mu_D(z,t)$ amplitude profile decays and broadens with time and does not depend on the sign of D. The phase profile $\theta_D(z,t)$ function, on the other hand, is an odd function of the dispersion parameter D. Plots of these profiles will be considered shortly.

It will prove useful at this point to consider the shape of the spatial phase profile for fixed time. This shape is defined by the second term on the right hand side of Eq. (15). For a positive D, the phase profile will be a parabola with a high point at $z=0$ and negative curvature. For a negative D, the phase profile will be a parabola with a low point at $z=0$ and positive curvature.

Turn now to the nonlinear response only case. Here, v_g, η, and D are set to zero and Eq. (10) reduces to

$$i\frac{\partial u}{\partial t}+N|u|^2u=0. \tag{16}$$

Subject to the initial condition of Eq. (12), Eq. (16) has a complex $u(z,t)$ nonlinear response only solution with the separate amplitude and phase functions $\mu(z,t)$ and $\theta(z,t)$ given by

$$\mu_N(z,t)=u_0e^{-z^2/4z_0^2} \tag{17}$$

and

$$\theta_N(z,t)=Nu_0^2te^{-z^2/2z_0^2}. \tag{18}$$

For this case, the wave packet amplitude function $\mu_N(z,t)$ stays precisely the same as specified by the initial profile. This is reasonable because there is no dispersion. The phase profile, however, is an odd function of the nonlinear parameter N, increases linearly with time, and has a spatial Gaussian shape of the same form as the square of the initial $u(z,t=0)$ profile. The form of Eq. (18) is consistent with simple considerations of an amplitude dependent frequency shift.

Figure 4 demonstrates the above results. The four graphs show plots of the solutions contained in Eqs. (14), (15), (17), and (18). The initial Gaussian pulse shape parameters u_0 and z_0 were set at $u_0=1\times10^{-2}$ and $z_0=0.021$ cm, respectively. This choice of z_0 would correspond to a pulse width at half power of 13 ns for $v_g=3.8\times10^6$ cm/s. This is a typical MSW situation.

The top plots show the square of the amplitude function, or $\mu(z,t)^2$, multiplied by 10^4, as a function of z for fixed t. For Fig. 4 and later figures, this $\mu(z,t)^2\times10^4$ vertical axis plot parameter will be denoted as the reduced power amplitude. The bottom plots are of the phase function $\theta(z,t)$ as a function of z for fixed t. Here, as well as in later figures, the vertical axis plot parameter will be denoted as phase.

The left side plots are for case (a) with $N=0$ and $D=\pm3\times10^4$ cm^2/rad s. The right side plots are for case (b) with $D=0$ and $N=\pm7.4\times10^9$ rad/s. The dashed line curve

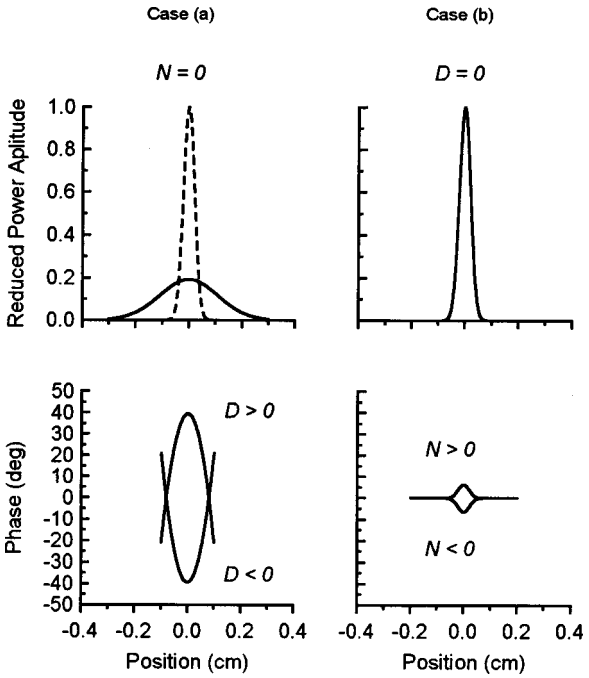

FIG. 4. The top left and right graphs show plots of the reduced power amplitude vs position z from Eqs. (14) and (17). The bottom left and right graphs show plots of the corresponding phase values vs position z from Eqs. (15) and (18). All graphs are based on an initial Gaussian pulse as defined through Eq. (12) with $u_0=1\times10^{-2}$ and $z_0=0.021$ cm. The dashed curve in the top left graph shows the initial reduced power amplitude vs z profile. The solid curves are all for $t=150$ ns. The solid amplitude and phase curves in the graphs on the left are for the case (a) scenario in the text for dispersion only, with $D=\pm3\times10^3$ cm^2/rad s and $N=0$. The solid curves in the graphs on the right are for case (b), with $N=\pm7.4\times10^9$ rad/s and $D=0$. The solid curves in the top graphs do not depend on the signs of D and N. The solid curves in the bottom graphs depend on the signs of D and N as indicated.

in the upper left graph shows the initial reduced power amplitude as a function of z at $t=0$. All of the solid curves show profiles at $t=150$ ns. Note that all profiles remain centered at $z=0$, due to the choice of a zero group velocity v_g for the analysis. The only effect of a nonzero v_g would be to produce a uniform translation of the center z value by v_gt. Keep in mind as well that the damping has been set to zero. There are no decay effects due to damping.

The graphs in Fig. 4 reinforce the observations from the equations. Consider the case (a), dispersion only and $N=0$ left side graphs first. From the upper left graph, it is clear that the power amplitude versus z profile at $t=150$ ns is broadened and reduced in amplitude relative to the initial profile. Only one solid curve is shown. The shape of the power amplitude profile is the same for both signs of the dispersion parameter D. The decay in amplitude and the broadening are a direct result of the nonzero dispersion. From the lower left graph, it is clear that the sign of the D parameter does have an important effect on the companion phase profiles. When D is positive, the phase profile has a maximum at $z=0$ and negative curvature. When D is negative, the phase profile has a minimum at $z=0$ and positive curvature.

The situation is different for the case (b), nonlinear response only and $D=0$ right side graphs. As shown in the

upper right graph, the power amplitude profile at $t=150$ ns is exactly the same as the initial pulse. Even though there are position dependent frequency shifts due to the nonzero N parameter, there is no broadening because there is no dispersion. These position dependent frequency shifts do show up in the phase profiles in the lower right graph. The phase profiles for the plus and minus values of N follow the same scenario as for the positive and negative values of D. When N is positive, the phase profile has a maximum at $z=0$ and negative curvature. When N is negative, the phase profile has a minimum at $z=0$ and positive curvature.

V. PROFILES FOR DISPERSIVE NONLINEAR PULSES

The results presented above considered the effects of dispersion and the nonlinear response separately. These results suggest that soliton formation involves phase change compensation when D and N have opposite signs. In order to examine this possibility directly, it is necessary to solve the NLS equation with both dispersion and the nonlinear response included in the analysis. When, however, both D and N are nonzero, it is not possible to obtain simple analytical expressions for the time and space dependent amplitude and phase profile functions $\mu(z,t)$ and $\theta(z,t)$, even for simple input pulse functions. In such situations, the NLS equation can best be solved numerically. This section presents some representative results for this problem. These phase compensation effects are demonstrated explicitly for Gaussian pulses. The numerical evaluations are done under the same zero group velocity and zero damping conditions as employed in Sec. IV, and the same choices for D and N are used. Similar results are found for hyperbolic secant and rectangular pulses.

The Fourier split step method used to solve the NLS equation is described in Ref. 21. The method is implemented by splitting the NLS equation into a linear and a nonlinear part and introducing a discrete time $t_n=n\cdot\Delta t$, where Δt is a time step parameter and the index n controls the time span for the simulation. For the calculations presented below, the step size Δt was chosen to be 0.1 ns. For a given initial profile, $u(z,t=0)$, the linear part of the NLS equation can be solved by discrete Fourier transform methods. The step size Δz which is used for this transform must be chosen in a way that so-called aliasing effects is avoided and the resulting pulse shape in Fourier space accurately represents the original $u(z,t=0)$ pulse in real space. For the results given below, Δz was taken as 0.0008 cm. The solution to the linear part of the NLS equation is then used as an initial condition to step forward the nonlinear part in time and obtain the solution at $t=\Delta t$. This $u(z,t=\Delta t)$ solution is then used as an initial condition for the next linear step and so on. In this way, the initial profile $u(z,t=0)$ can be stepped forward in time to obtain a series of $u(z,t_n)$ profiles which converge, in principle, to some solution $u(z,t)$ at $t=t_n$ if Δt is chosen small enough. The Δt value of 0.1 ns was found to be small enough to yield good convergence and still keep the computation time within practical limits for a standard personal computer. The numerical results were checked against the analytic solutions obtained in the previous section and for the well known hyperbolic secant single soliton solution to the NLS equation obtained from inverse scattering.[22]

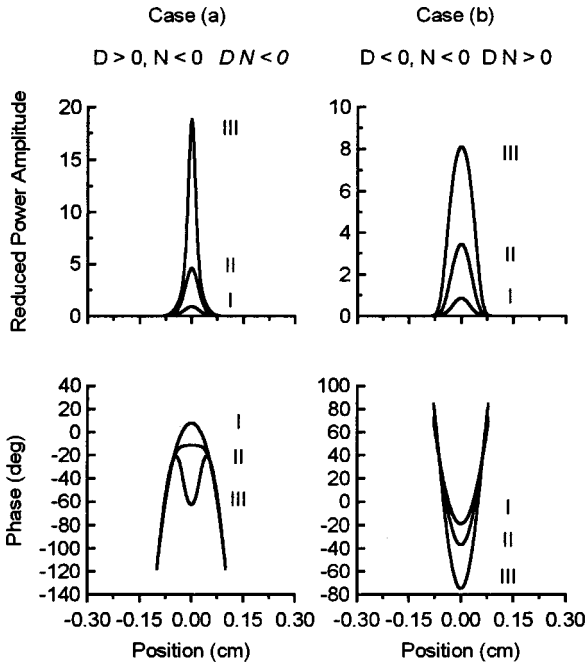

FIG. 5. The top left and right graphs show plots of reduced power amplitude vs position z. The bottom left and right graphs show corresponding plots of phase vs position z. All graphs are based on an initial Gaussian pulse as defined through Eq. (12) with $z_0=0.021$ cm. The labels I, II, and III for the solid curves in each graph designate output profiles for $u_0=0.01$, $u_0=0.021$, and $u_0=0.035$, respectively. All curves are for $t=150$ ns. All curves were obtained by numerical solution of the NLS equation with the group velocity and damping parameters ν_g and η set to zero. All graphs are for a nonlinear response coefficient $N=-7.4\times10^9$ rad/s. The amplitude and phase plots in the left side graphs under case (a) are for $D=+3\times10^4$ cm^2/rad s, such that the condition $DN<0$ is satisfied. The amplitude and phase plots in the right side graphs under (b) are for $D=-3\times10^4$ cm^2/rad s, such that the condition $DN>0$ is satisfied.

Figure 5 shows the results of the numerical NLS evaluations for a Gaussian input pulse. The format and layout of the figure is similar to that of Fig. 4. The top plots show reduced power amplitude as a function of z for fixed t. The bottom plots show the phase as a function of z for fixed t. All plots are based on a negative nonlinear response coefficient, $N=-7.4\times10^9$ rad/s. The left side plots under case (a) are for a positive dispersion coefficient $D=+3\times10^4$ cm^2/rad s, so that the Lighthill criterion for soliton formation, $DN<0$ is satisfied. The right side plots under case (b) are for $D=-3\times10^4$ cm^2/rad s, so that the Lighthill criterion is not satisfied. The Gaussian width parameter for the input pulses was kept at $z_0=0.021$ cm. The output profiles were all evaluated for a net time evolution of 150 ns, and the group velocity ν_g and the relaxation rate η were both set to zero. These conditions all match the conditions used in Sec. IV. Calculations were done for three values of the input pulse amplitude u_0. The solid curves and the labels I, II, and III for each graph in Fig. 5 designate the output profiles for $u_0=0.01$, $u_0=0.021$, and $u_0=0.035$, respectively.

The situation when both D and N are nonzero lead to important differences for both power amplitude and phase profiles which depend on the sign of the DN product. Con-

sider the power amplitude profiles first. For case (a) and $DN<0$, increasing values of u_0 result in an increase in the amplitude of the propagated pulse, as expected. It also results in a clear narrowing and steepening of the wave packet. The steepening and narrowing in the amplitude response goes hand in hand with the evolution in the phase profiles shown in the lower left case (a) graph. The phase evolves from a dispersion dominated profile at I, to a compensated phase profile over the pulse center at II, to a nonlinear response dominated profile at III. As will be shown in Sec. VI, phase measurements show plateau regions over certain power ranges for MSBVW pulses which indicate the formation of MME solitons.

Turn now to case (b) and the $DN>0$ situation. Here, increasing values of u_0 also result in an increase in the amplitude of the propagated pulse. However, these increasing initial amplitudes now result in increased broadening of the propagated signal as well. There is no steepening and narrowing of the sort which is in clear evidence from the case (a) power amplitude profiles. The accompanying phase profiles, moreover, do not change in character nor do they show any compensation effect. The negative peaks and positive curvature phase profiles simply become more and more accentuated. From the results of Sec. IV, this is to be expected. The negative D and the negative N both produce this type of phase profile. The increase in u_0 leads to an increase in the nonlinear contribution to this phase response.

It is noteworthy that for case (a) in Fig. 5, even when the amplitude is set properly as for II, the phase profile is constant only across the very center of the corresponding power amplitude profile. This localized region of fixed phase is closely related to the choice of a Gaussian shape for the input pulse. The tails of the Gaussian correspond to low amplitudes. In these tail regions, the phase character is dominated by the dispersion and is positive going. The negative going phase peak character associated with negative N is effective in compensating the phase response only over the large amplitude region near the pulse center.

It is useful to contrast the results in Fig. 5 with results for an input pulse shape with the functional dependence of an hyperbolic secant. The hyperbolic secant functional form is known to provide an analytic solution to the NLS equation in the limit $\eta=0$.[23] This occurs when the reduced amplitude of the hyperbolic secant input pulse, u_0, is set equal to $[2\ln(\sqrt{2}+1)/\Gamma]\sqrt{|D/N|}$, where Γ is the spatial half width of the power amplitude $[u(z,t)]^2$ profile. The reader may easily verify that the corresponding order one soliton function,

$$u_s(z,t)=u_0\ \mathrm{sech}\left[u_0\sqrt{\left|\frac{N}{D}\right|}(z-\nu_g t)\right]e^{1/2iu_0^2Nt}, \tag{19}$$

is an exact solution to Eq. (10) if η is set to zero. It is important to emphasize that Eq. (19) is soliton specific. The width of the soliton pulse is proportional to $\sqrt{|D/N|}/u_0$ according to the form of Eq. (19). Note that the soliton amplitude function $u_s(z,t)$ has no spatial phase term. It does have a linear temporal phase.

The hyperbolic secant numerical simulations were done for an unrestricted input profile function of the form,

$$u(z,t=0)=u_0\ \mathrm{sech}(z/z_h), \tag{20}$$

where the parameter z_h now controls the spatial width of the initial profile independent of the amplitude u_0. Simulations were done for three u_0 values, one below, one above, and one precisely at the critical amplitude for solitons implicit in Eq. (19). The width parameter z_h was held fixed.

The amplitude and phase profiles for hyperbolic secant pulses follow the basic scenario given above for the Gaussian pulse. When the condition $DN<0$ is satisfied, the phase profile starts out as a positive going peak with negative curvature when u_0 is small and becomes negative going with positive curvature when u_0 is large. The calculated phase profile curves have the same basic appearance as the curves in the lower case (a) diagrams of Fig. 5, but with one difference. If one chooses the particular soliton specific value of u_0 which corresponds to the chosen width parameter z_h in order to calculate curve II, the phase change across the pulse is precisely zero.

The final example to be considered in this section is the rectangular input pulse case. This is the case which is closest to the experimental situation, since the input microwave pulses used for typical MME soliton experiments are rectangular pulses with widths in the 10–30 ns range:

Numerical analysis for rectangular input pulses show the same basic phase effect as the other shapes when the condition $DN<0$ is satisfied. Small u_0 values give positive going phase profiles with negative curvature. Large u_0 values give negative going phase profiles with positive curvature. A properly chosen intermediate u_0 value gives a region of constant phase across the center region of the pulse. For the rectangular pulse, this center region is wider than for the Gaussian example but does not extend over the entire power amplitude profile as found for the hyperbolic secant shape. This evolution in phase profiles is accompanied by a pronounced steepening and narrowing of the power amplitude profiles, as for the other cases. The specific response curves are similar in nature to those shown in Fig. 5.

The above results demonstrate the effect of phase change compensation when the Lighthill criterion is satisfied, and the steepening and narrowing of the amplitude profiles which accompanies this phase compensation. The analysis so far, however, has been purely theoretical and somewhat idealized. Keep in mind that the amplitude and phase profiles were obtained only in the limit of zero damping and for stationary pulses. The next section will present experimental results for MSBVW and MSSW pulses which demonstrate the phase compensation effects shown above.

VI. EXPERIMENTAL PROFILES AND PHASE COMPENSATION

The purpose of this section is to demonstrate the phase compensation effects presented above with actual MME pulse data. The measurement procedures are discussed in detail in the references cited above. This section will focus on two types of MME pulse measurements which parallel the previous discussion, (i) the MSBVW case for which the Lighthill criterion is satisfied and MME bright solitons are obtained at sufficient input power levels, and (ii) the MSSW

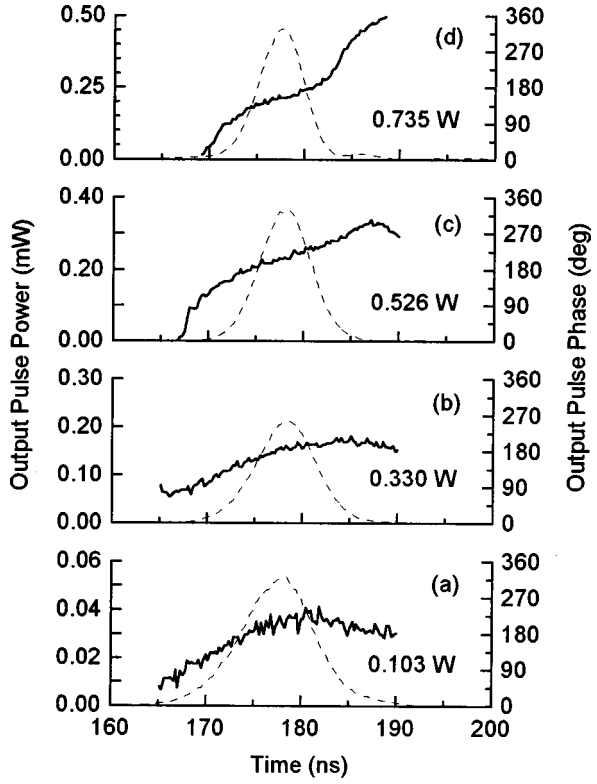

FIG. 6. Experimental phase and power profiles for a MSBVW signal detected at the output of a transducer structure of the sort shown in Fig. 1. The solid lines show phase and the dashed lines show power. The input pulse width was 10 ns and the carrier frequency was 5.8 GHz. Graphs (a)–(d) are for increasing values of the input power as indicated.

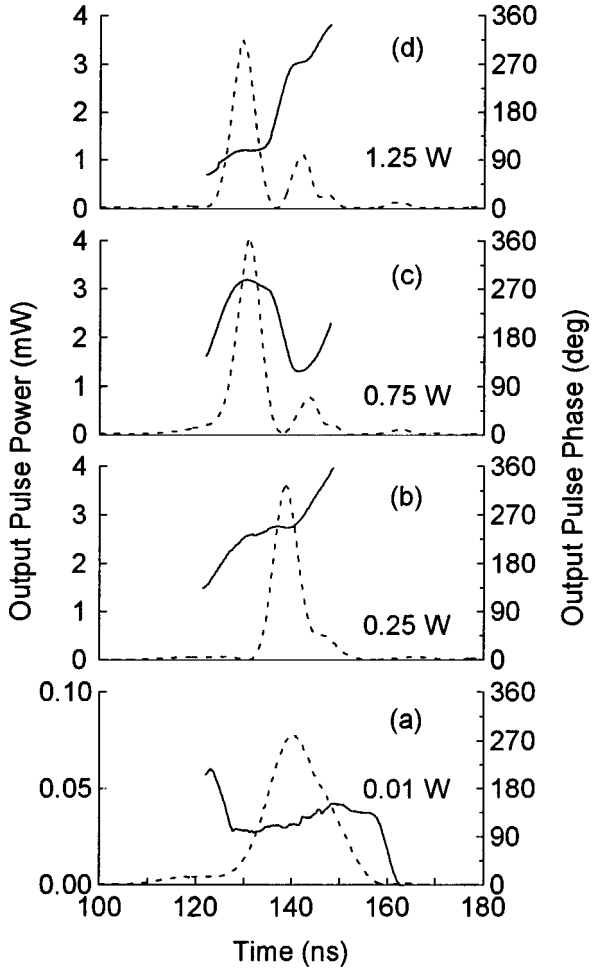

FIG. 7. Experimental phase and power profiles for a MSBVW signal detected at the output of a transducer structure of the sort shown in Fig. 1. The YIG film thickness was 7.2 μm. The solid curves show phase and the dashed curves show power. The input pulse width was 26 ns, the carrier frequency was 5.0 GHz, and the static field was 1.088 kOe. Graphs (a)–(d) are for increasing values of the input power as indicated.

case for which the Lighthill criterion is not satisfied and bright solitons are not obtained. Many of the details contained in the earlier MME soliton references are omitted here. The focus is on the experimental phase profiles for these bright pulse situations and the correlation with theory.

Typical experiments involve rectangular temporal input pulses applied to an input transducer and temporal output pulses detected at an output transducer. The experimental results, therefore, consist of plots of power and phase versus time rather than position. The time scales are also shifted, since these real pulses propagate at a specific group velocity which is controlled by the experimental conditions. Typical arrival times at the output transducer, relative to the launch time, are in the 100–200 ns range.

Figure 6 shows a series of four power profiles and phase profiles for MSBVW pulses generated at the output antenna of a transducer structure of the type shown in Fig. 1. The YIG film was 7.2 μm thick. The carrier frequency was 5.8 GHz and the in-plane static external magnetic field was 1.343 kOe. The input pulse width was 10 ns. The propagation distance from launch was 4 mm. The peak input powers are increasing from graphs (a)–(d) and had the values indicated. The power and phase profiles are indicated by dashed lines and the solid lines, respectively.

The data in Fig. 6 follow the scenario established in the previous sections. Recall that the dispersion coefficient D is positive for MSBVW signals, the nonlinear response coefficient N is negative, and the Lighthill criterion is satisfied. Solitons are expected.

For the lowest power level situation in graph (a), the output power pulse profile is accompanied by a phase profile which has a positive going peak and negative curvature. This phase profile is not as pronounced as the simulations in the last section, presumably due to the presence of damping. As the power level is increased and one moves up to graph (b) and then to graph (c) and graph (d), the flattening out of the phase response is clear. Here too, the effect is not as pronounced as shown by the basic decay free narrow pulse simulations of the last section. The phase compensation with increasing power is clear, nevertheless.

The relatively short input 10 ns pulse width for the data in Fig. 6 was needed to bring out the dispersion dominated phase response at low powers. In order to accentuate, the flat phase response is realized in the soliton regime. Similar data were obtained for a wider input pulse width of 26 ns. These data are shown in Fig. 7. The details were not exactly the same as for the Fig. 6 data. The same 7.2-μm-thick film was used. In this case, however, the carrier frequency was 5.0

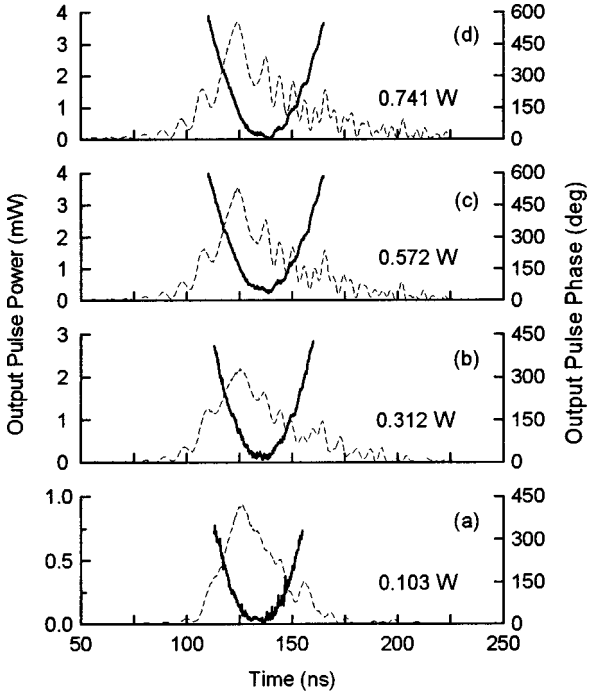

FIG. 8. Experimental phase and power profiles for a MSSW signal detected at the output of a transducer structure of the sort shown in Fig. 1, but with the in-plane magnetic field **H** perpendicular to the MSSW propagation direction. The YIG film thickness was 4.8 μm. The solid curves show phase and the dashed curves show power. The input pulse width was 10 ns, the carrier frequency was 5.1 GHz, and the static field was 1.070 kOe. Graphs (a)–(d) are for increasing values of the input power as indicated.

GHz and the static field was 1.088 kOe. The format of the figure is the same as for Fig. 6. Graphs (a)–(d) are for increasing values of the input power. The solid lines show the phase profiles and the dashed lines show the companion power profiles.

It is clear that the power profile in the bottom graph of Fig. 7 is broader than the rest. This is one indication that a soliton has not formed. The phase profile is irregular and is not particularly indicative of the expected dispersion dominated phase character. This is a result of the significantly wider input pulse width of 26 ns, relative to the experimental situation for Fig. 8 or the simulations in Sec. V.

Graph (b), for an input power of 0.25 W, shows a power profile which has narrowed and steepened considerably. This profile is accompanied by a phase profile which shows a flat response over the center portion of the power profile. Both of these effects provide indications of soliton formation. The flat phase response is in accord with the results of Sec. V. It is also important to note the pronounced shoulder on the right side of the power profile. This shoulder is the beginning of a second peak associated with an order two soliton.

Graph (c) in Fig. 7 shows an intermediate response profile which is clearly above the order one soliton threshold. The power profile for the main peak has about the same width as in (b) and the amplitude has not increased, in spite of the factor of three increase in the input power. The additional energy is manifested in the second peak which has evolved from the shoulder noted above. The phase profile is concave downward for the main peak and concave upward for the second smaller peak.

Graph (d) is for the highest peak power level used for these measurements. Both peaks now appear to have stabilized. The phase profile curve is particularly interesting here. The flat response region across the main peak has returned and a *second* flat region across the second smaller peak has formed. Graph (d) provides a striking demonstration of the zero phase change effect in the context of a multisoliton response.

As a last experimental example, consider the case of MSSW pulse propagation. Here, the Lighthill criterion is not satisfied and one expects to see phase profiles of the sort shown in the lower right graphs of Fig. 5. Some representative MSSW data are shown in Fig. 8. The configuration was the same as shown in Fig. 1, except that the in-plane static magnetic field **H** was perpendicular to the propagation direction. The film thickness for these data was 4.8 μm. The carrier frequency was 5.1 GHz and the static field was 1.070 kOe. The format of the figure is the same as for Figs. 6 and 7. Graphs (a)–(d) are for increasing values of the input power. The solid lines show the phase profiles and the dashed lines show the corresponding power profiles.

The same basic amplitude character is evident from all four graphs in Fig. 8. Apart from some additional structure on the envelope, there is no significant change in shape as the power is increased. At the same time, the same basic phase character is evident from all the graphs. All phase profiles show negative going peaks and are concave upward. The overall size of the phase change across the pulse increases somewhat with power. Just as the data of the previous two figures demonstrate phase compensation for soliton formation when the Lighthill criterion is satisfied, the data in Fig. 8 demonstrate the lack of such compensation and no soliton formation when this condition is not satisfied.

VII. SUMMARY AND CONCLUSION

The effects of dispersion and the nonlinear response has been examined both analytically and numerically, based on the formalism of the nonlinear Schrödinger equation and propagation parameter values which correspond to microwave magnetic envelope wave packets formed from magnetostatic backward volume waves and magnetostatic surface waves. When these effects are considered separately, they lead to phase profiles which suggest the possibility of compensation. That is, positive values of either D or N yield positive going peaks with negative curvature, while negative values yield negative going peaks with positive curvature.

When both D and N are nonzero, one does obtain phase compensation at particular values of the pulse amplitude when these parameters are of opposite sign. This phase compensation when the condition $DN<0$ is satisfied provides a new perspective on the criteria for MME soliton identification and the Lighthill criterion. The compensation effect is demonstrated for Gaussian, hyperbolic secant, and rectangular pulse shapes. These theoretical results are supported by measurements on MSBVW and MSSW pulse signals.

ACKNOWLEDGMENTS

This work was supported in part by the National Science Foundation under Grant Nos. DMR-8921761 and DMR-9400276 and by the U.S. Army Research Office under Grant No. DAAH04-95-1-0325. Professor Kabos is on leave from Faculty of Electrical Engineering and Information Technology, Slovak Technical University, Bratislava, Slovakia.

[1] A. K. Zvezdin and A. F. Popkov, Zh. Eksp. Teor. Fiz. **84**, 606 (1983); Sov. Phys. JETP **57**, 350 (1983).
[2] B. A. Kalinikos, N. B. Kovshikov, and A. N. Slavin, Pis'ma Zh. Eksp. Teor. Fiz. **38**, 343 (1983); JETP Lett. **38**, 413 (1983).
[3] P. De Gasperis, R. Marcelli, and G. Miccoli, Phys. Rev. Lett. **59**, 481 (1987).
[4] B. A. Kalinikos, N. B. Kovshikov, and A. N. Slavin, Zh. Eksp. Teor. Fiz. **94**, 159 (1988); Sov. Phys. JETP **67**, 303 (1988).
[5] B. A. Kalinikos, N. G. Kovshikov, and A. N. Slavin, IEEE Trans. Magn. **26**, 5 (1990).
[6] M. Chen, M. A. Tsankov, J. M. Nash, and C. E. Patton, Phys. Rev. Lett. **70**, 1707 (1993).
[7] M. Chen, M. A. Tsankov, J. M. Nash, and C. E. Patton, Phys. Rev. B **49**, 12 773 (1994).
[8] M. A. Tsankov, M. Chen, and C. E. Patton, J. Appl. Phys. **76**, 4274 (1994).
[9] B. A. Kalinikos and N. G. Kovshikov, Pis'ma Zh. Eksp. Teor. Fiz. **60**, 290 (1994); JETP Lett. **60**, 305 (1994).
[10] J. M. Nash, C. E. Patton, and P. Kabos, Phys. Rev. B **51**, 15 079 (1995).
[11] J. M. Nash, P. Kabos, and C. E. Patton, 1995 Digests of Intermag'95, IEEE Cat. No. 95CH35782, 1995 (unpublished), p. AD-1.
[12] N. G. Kovshikov, B. A. Kalinikos, C. E. Patton, E. S. Wright, and J. M. Nash, Phys. Rev. B **54**, 15 210 (1996).
[13] J. M. Nash, P. Kabos, and C. E. Patton, 1996 Digests of Intermag'96, IEEE Cat. No. 96CH35912, 1996 (unpublished), p. AE-03.
[14] H. Xia, P. Kabos, C. E. Patton, and E. E. Ensle, Phys. Rev. B **55**, 15 018 (1997).
[15] B. A. Kalinikos, N. G. Kovshikov, and C. E. Patton, Phys. Rev. Lett. **78**, 2827 (1997).
[16] R. W. Damon and J. R. Eshbach, J. Phys. Chem. Solids **19**, 308 (1961).
[17] R. W. Damon and H. van de Vaart, J. Appl. Phys. **36**, 3453 (1965).
[18] M. J. Lighthill, J. Inst. Math. Appl. **1**, 269 (1965).
[19] M. J. Hurben and C. E. Patton, J. Magn. Magn. Mater. **163**, 39 (1996).
[20] C. Kittel, Phys. Rev. **73**, 155 (1948).
[21] T. R. Taha and M. J. Ablowitz, J. Comput. Phys. **55**, 203 (1984).
[22] M. J. Ablowitz and H. Segur, *Solitons and the Inverse Scattering Transform* (SIAM, Philadelphia, 1981).
[23] V. E. Zakharov and A. B. Shabat, Zh. Eksp. Teor. Fiz. **61**, 118 (1971); Sov. Phys. JETP **34**, 62 (1972).